Enhanced Densification and Conduction Properties of $Li_{5+x}La_3Nb_{2-x}Zr_xO_{12}$ Garnet Solid-State Electrolytes through Zn Doping on the Nb/Zr site

Bo Dong[†,], Linhao Li[‡], Xiao Tao[§], Mark P. Stockham, Chuan Li[⊥], Yongliang Li[⊥], Yulong Ding[⊥], Peter R. Slater[†,*]*

†School of Chemistry, University of Birmingham, B15 2TT
‡Department of Materials Science and Engineering, University of Sheffield, S1 3JD
§ School of Metallurgy and Materials, University of Birmingham, B15 2TT
⊥School of Chemical Engineering, University of Birmingham, B15 2TT

*b.dong@bham.ac.uk; p.r.slater@bham.ac.uk;

Keywords: Garnet; Solid State Electrolyte; Zn doping; Densification

Abstract

While garnet Li ion conductors are attracting considerable interest as potential solid state electrolytes for Li ion batteries, a key challenge is to improve the conductivity, which is associated with the Li content in the structure, and to overcome the challenges of sintering dense electrolyte membranes. In this work we show that Zn doping on the 16a octahedral Nb site leads to substantially improved sintering in both $Li_5La_3Nb_2O_{12}$ and $Li_6La_3ZrNbO_{12}$. As a result of the enhanced sintering, and the associated increase in Li content, the conductivities in both garnet systems were significantly enhanced on Zn doping, up to 2.1 x 10^{-4} Scm^{-1} at 25 ^oC for $Li_{6.6}La_3ZrNb_{0.8}Zn_{0.2}O_{12}$. This doping strategy therefore represents a promising approach to improve the relative density and, hence, ionic conductivity of garnet solid state electrolyte materials for possible solid-state battery applications.

Introduction

State-of-the-art lithium ion batteries (LIBs) dominate the energy storage market due to their high energy density and long cycle life compared to other energy storage systems[1]. However, commercial LIBs often use liquid electrolytes (such $LiPF_6$ in EC/DEC organic solvent), which have a variety of safety, thermal and toxicity concerns, some of which are uniquely problematic in the emerging electric vehicle market[2, 3]. It is thought these concerns can be addressed by use of an all-solid-state battery (ASSB), where the flammable electrolyte is replaced with an inorganic solid-state electrolyte (SSE). Additionally, ASSBs would also allow higher energy density cells by enabling use of high-performance cathode materials and anodic lithium metal. Therefore SSEs have attracted considerable attention in the field of next generation LIBs[4, 5]. Over the last few decades, various potential SSEs have been investigated, including LISICON[6-8], NASICON[9, 10], perovskites[11], garnet[12], Thio-LISICON[13], argyrodite[14] and anti-perovskites[15]. However, of all the systems reported, the lithium garnet systems are among the few which encompass both good electrochemical stability and high room temperature Li^+ ion conductivity. Hence the garnet solid-state electrolytes are envisaged as promising candidates for all-solid-state batteries.

The ideal garnet has a general formula $A_3B_2C_3O_{12}$ where A, B and C are 8, 6 and 4 oxygen coordinated metal ions. The garnet has a cubic structure ($Ia\bar{3}d$), which contains a framework of corner-linked tetrahedra and octahedra

with the larger A ions located in cavities[12, 16]. In 2003, the first report of high Li^+ ion conductivity was made by Thangadurai et al. for $La_3M_2Li_5O_{12}$ (M = Nb, Ta). Later studies into the conductivity mechanism revealed lithium ions were located in the tetrahedral site (24d), as well as distorted interstitial octahedral sites (48g and 96h)[17]. Further work determined that, in addition to lithium content, lithium ion distribution is key in understanding, and optimizing, the Li^+ ion conductivity of the garnet SSEs[18]. Subsequent work has employed a variety of aliovalent doping strategies to improve the conductiviry to $>10^{-4}$ S cm^{-1}, including substitution at the A site (Ca, Ba), B site (Zr, Hf, Sn) and C site (Al, Ga)[19-26].

The maximum lithium content was demonstrated to be 7 as shown for $Li_7La_3Zr(Hf, Sn)_2O_{12}$ garnets, although in these system the lithium ions are ordered in three fully occupied sites (tetrahedral 8a and octahedral 16f and 32g sites), leading to tetragonal systems with lower conductivity[27-29]. High temperature X-ray diffraction study shows a reversible tetragonal to cubic phase transition in $Li_7La_3Zr_2O_{12}$ at 750 ^oC[30]. This cubic phase with much higher conductivity can be obtained at lower temperature by the incorporation of lithium vacancies, either through Li loss during high temperature synthesis or reaction with alumina crucibles resulting in Al incorporation. In addition, proton/lithium exchange in tetragonal garnet has also been shown to form cubic symmetry, whereby moisture reacts to form a LiOH surface layer, which subsequently reacts with CO_2 to form a Li_2CO_3 insulating layer[31, 32]. The quest

to utilise these electrolytes in practical ASSBs has meant that interfacial issues, like high electrolyte - cathode/anode interfacial resistance, dendrite propagation through the solid state electrolyte, have attracted more attention in recent years[33-35]. The interfacial resistance can be negated somewhat via a surface coating that subsequently forms a Li metal alloy. This also prevents dendrite growth by acting as a buffer layer[36, 37]. Polymer – garnet ceramic composites have also been shown to address the interfacial problems while also eliminating high temperature sintering[38, 39].

However, a major challenge still remains; the densification of the electrolyte membrane, which is essential for high Li^+ ion conductivity and the mechanical stability of the garnet SSE. Typical sintering conditions of garnet pellets consist of very high temperature (~1200 ^oC) and long sintering time (12 – 24 h). This high temperature process results in lithium loss and so excess (typically >20% mol excess) Li is needed, in addition to the pellet being covered with mother powder from the same pellet to limit lithium evaporation[40, 41]. Even these strategies commonly lead to too much Li loss and hence the formation of impurity phases. Consequently, significant interest has developed to find alternate strategies to improve the densification process. Ceramic sintering techniques with additional driving force for sintering, such as hot-pressing and spark plasma sintering[42, 43], have shown decreased sintering temperature and can shorten the sintering time to 1 h. However, these techniques are costly and difficult to scale-up for production. In addition, more

practical approaches have considered use of sintering aids as a densification strategy, such as Al_2O_3, Ga_2O_3, Li_3BO_4, Li_4SiO_4[44, 45]. The issue of these sintering aids is the reaction with garnet, consequently leading to the generation of a non-stoichiometric garnet and potentially other impurity phases.

There has been prior work on Zn^{2+} incorporation $Li_7La_3Zr_2O_{12}$, where substitution on the 24d tetrahedral Li^+ site was reported[46]. Attempts to dope Zn on the 96d octahedral site to give a Li excess material of formula $Li_{7+2x}La_3Zr_{2-x}Zn_xO_{12}$ was also investigated, but impurities were observed for all samples and no conclusive confirmation of Zn incorporation on the Zr site[47]. This can be explained by the inability to accommodate more than 7 Li ions in these garnet systems. However, no attempts have been made to dope Zn on the 16a octahedral site in garnets with Li contents lower than 7. In this work, Zn^{2+} dopant was therefore used to substitute onto the 16a octahedral Nb^{5+} ions for the first time in $Li_{5+x}La_3Nb_{2-x}Zr_xO_{12}$ and the corresponding effects on relative density, electrical and electrochemical properties were studied. These studies show the first successful Zn incorporation onto this site, and these Zn doped garnets show a dramatic increase in density at shorter sintering time, in addition to the associated enhanced Li^+ ion conductivity due to the resultant increase in Li content.

Experimental

Synthesis

Li_2CO_3 (99.9%, Alfa Aesar), ZrO_2 (99.9%, Sigma Aldrich), La_2O_3 (99.9%, Sigma Aldrich), Nb_2O_5 (99%, Sigma Aldrich) and ZnO (99%, Sigma Aldrich) were used as starting materials. Li_2CO_3 was dried at 180 ^oC while ZnO, ZrO_2 and Nb_2O_5 were dried at 900 ^oC before use. $Li_{5+3x}La_3Nb_{2-x}Zn_xO_{12}$: x = 0, 0.1, 0.2, 0.3, 0.4, 0.6 and $Li_{6+3x}La_3ZrNb_{1-x}Zn_xO_{12}$: x = 0, 0.2 samples were prepared via the solid state route by intimate grinding of stoichiometric amounts of reagents. The powders were then initially heated to 650 ^oC for 12 hours at 5 $^oC\ min^{-1}$. To compensate for Li loss during the heat treatment/sintering, 10-15% excess Li_2CO_3 were a then added to the powders, which were subsequently ball milled (ZrO_2 containers and balls) with hexane for 30 minutes (FRITSCH Pulverisette 7 classic line planetary ball mill). The fine powders were uniaxially pressed into pellets, placed onto ZrO_2 pellets to prevent Al contamination and reheated at 1000-1050 ^oC for 12 hours at 5 $^oCmin^{-1}$ to yield the final product.

Characterisation of Materials

X-ray diffraction data were collected using a Bruker D8 X-ray diffractometer (XRD) (CuKα radiation) with a linear position sensitive detector. Patterns were recorded over 2θ range 15^o to 80^o with a 0.02^o step size. Structural refinement was carried out using the GSAS suite of Rietveld refinement software.

Scanning electron microscopy (SEM, Philips/FEI XL 30S FEG) was employed to examine the microstructure. Before being coated with carbon, bulk samples were polished and thermally etched at 90% of the sintering

temperature for 1 h. Powder samples were fixed on conductive carbon tapes. An accelerating voltage of 5 kV and an effective spot size of 3 mm was used. The distribution of elements was probed with an energy dispersive X-ray spectroscopy (EDX) detector.

Pellets for impedance measurements were sintered at 1000-1100°C for 4 hours at a heating rate of 5 $^{o}Cmin^{-1}$ in dry N_2. The pellet was placed on, and covered with, mother powders to suppress Li_2O loss and prevent any reaction with the Al_2O_3 crucible. Au paste was painted on both sides of the pellet and heated at 850 ^{o}C for 1 hour. Impedance data were recorded in air with a HP 4192 analyser with 100 mV A.C. applied voltage over the frequency range 1 to 10^7 Hz.

Electrochemical Characterisation

Li metal and stainless steel (SS) were chosen as working and counter electrodes respectively. A Li//$Li_{6.6}La_3ZrNb_{0.8}Zn_{0.2}O_{12}$(LLZNZ)//SS cell was assembled with a split cell in an Argon filled glove box. The electrochemical stability window was tested using a Biologic SP150 potentiostat by CV technique over the range -0.4 to 6 V with a 1 mVs^{-1} scan rate.

Results and discussion

Phase formation

$Li_5La_3Nb_2O_{12}$ is indexed using a cubic $Ia\bar{3}d$ cell as previously reported for cubic garnet electrolytes. Given the lower charge of Zn (2+) versus Nb (5+),

for charge balance the incorporation of an extra 3 Li^+ are required, giving a general formula $Li_{5+3x}La_3Nb_{2-x}Zn_xO_{12}$. Thus, Zn doping leads to a significant increase in the Li content of the sample (3 extra Li^+ ions introduced per 1 Zn^{2+} incorporation in place of Nb^{5+}). As shown in figure 1, the XRD patterns for $Li_{5+3x}La_3Nb_{2-x}Zn_xO_{12}$ show single phase samples for x = 0 - 0.2 compositions, with a linear increase in cell parameters as a function of composition until x = ~ 0.3 (figure 2), implying the formation of a solid solution across this range and corresponding to Vegard's law. The observed cell expansion is in agreement with replacing Nb^{5+} ions with larger Zn^{2+} ions (ionic radius of 0.64 and 0.74 for Nb^{5+} and Zn^{2+} respectively in a 6-oxygen coordinated octahedral site). Above x = 0.3, $LiNbO_3$, $ZnNb_2O_6$, La_2O_3 impurity phases became increasingly apparent. Hence x = 0.3 is thought to be the Zn limit for these systems, which is supported by the lack of any significant change in cell parameters for compositions between x = 0.4 and 0.6.

As optimum garnet Li conductivities are typically found in compositions with Li content between ~ 6.4 - 6.6, Zn doping in the $Li_6La_3ZrNbO_{12}$ system was subsequently investigated to see if sintering and Li ion conductivity could be improved. As shown in figure 3, a single cubic phase was observed for $Li_{6.6}La_3ZrNb_{0.8}Zn_{0.2}O_{12}$ (LLZNZ). Structure refinement of these phases were carried out using XRD data to confirm the replacement of Zn^{2+} on Nb^{5+} site. As XRD is insensitive to lithium in the presence of heavy elements, the atomic coordinates, occupancies and U_{isos} of lithium atoms were constrained as the

same. Given that Zr^{4+} and Nb^{5+} are isoelectronic, a constraint between Nb1 and Zr1 was set with the occupancies in the ratio (1:1) in accordance to the chemical composition for $Li_6La_3ZrNbO_{12}$. The Uiso parameters of all atoms were initially set to a typical value of 0.01 Å. The scale factor, background (6 terms of shifted Chebyshev function) and lattice parameters were refined at the beginning, followed by peak profile parameters and 2θ zero error which were refined and fixed at the converged value. Finally, the atomic coordinates of O1, U_{isos} of La1, Nb1(Zr1) were refined together in the last step. The refined parameters for $Li_6La_3ZrNbO_{12}$ are summarised in table 1.

Similar refinement strategy was applied to $Li_{6.6}La_3ZrNb_{0.8}Zn_{0.2}O_{12}$. Zn1 was added as the same atomic position of Zr1/Nb1 with a total occupancy for Zn1 and Nb1 of 0.5. This refinement gave occupancies of 0.40(1) for Nb1 and 0.10(1) for Zn1 which is consistent with the expected composition. The final refined parameters for $Li_{6.6}La_3ZrNb_{0.8}Zn_{0.2}O_{12}$ are shown in table 2.

The relative densities of both the Zn doped $Li_5La_3Nb_2O_{12}$ and $Li_6La_3ZrNbO_{12}$ pellets (Table 1) show dramatic improvement compared with undoped samples: the relative densities of $Li_{5.6}La_3Nb_{1.8}Zn_{0.2}O_{12}$ and $Li_{6.6}La_3ZrNb_{0.8}Zn_{0.2}O_{12}$ increased to 87% and 90% compared to $Li_5La_3Nb_2O_{12}$ and $Li_6La_3ZrNbO_{12}$ (61% and 59%) under the same synthesis/sintering conditions. This is consistent with prior studies in other fields (e.g. perovskite proton conductors), where Zn doping has been shown to be an excellent sintering aid[48, 49]. The following part of the paper focuses on LLZNZ sample as

it showed highest ionic conductivity (see later).

The surface microstructure of a LLZNZ pellet was characterised by SEM, as shown in figure 4. A dense garnet pellet with a few small pores was observed, confirming Zn ions are a good densification dopant for garnet solid state electrolyte materials. The grain size distribution for LLZNZ is in the range ~ 2 – 10 μm with no detection of impurities at the grain boundary. The EDX mapping shows a homogeneous distribution of La, Zr, Nb, Zn and O through the sample consistent with its incorporation into the structure in agreement with the Rietveld refinement data.

Conductivity Results

Typical impedance data for $Li_{6.6}La_3ZrNb_{0.8}Zn_{0.2}O_{12}$ are shown in figure 5. In the Z* complex plot (5a), a high frequency arc which passes the origin point and a low frequency spike were observed. A resistor R1 in parallel with a constant phase element CPE1 were used to fit the semicircle while another CPE2 which is in series with R1/CPE1 accounted for the sharp spike.

The corresponding spectroscopic C' plot (5b) shows a high frequency plateau with a capacitance of 8.7 $pFcm^{-1}$ which is a typical value for the bulk response with an associated permittivity of 10 – 20 (assuming A/l = 10)[50]. At lower frequencies, a plateau with a capacitance of 1.3 μFcm^{-1} was observed; this high capacitance is a good indication of double layer effect at the sample – electrode interface with Li^+ ion conduction in this case.

Plots of log Y' as a function of log f (5c) show a frequency independent

plateau at intermediate frequency, which corresponds to the bulk conductivity. A dispersion at high frequency related to the Jonscher's power law and a curvature at low frequency representing the blockage of Li ions at the electrode – sample interface are detected[51].

From the Arrhenius plot (figure 6), the conductivities of Zn doped $Li_5La_3Nb_2O_{12}$ show an improvement compared to undoped $Li_5La_3Nb_2O_{12}$. Similar enhanced conductivities are observed for Zn doping in $Li_6La_3ZrNbO_{12}$. As shown in figure 7, the conductivity of LLZNZ reached 2.1 x 10^{-4} Scm^{-1} at 25 ^oC with an associated activation energy of 0.39(1) eV. Such conductivity is ~ two orders more than $Li_6La_3ZrNbO_{12}$ (without Zn doping) that was prepared and sintered under the same conditions

Electrochemical Properties

The electrochemical stability and durability of LLZNZ was tested using a SS/LLZNZ//Li cell by CV in the voltage range -0.4 to 6 V. Two redox peaks around 0 V were detected, this represents lithium stripping and plating as shown in previous studies. No additional redox peaks were observed in the whole range supporting that LLZNZ has a wide electrochemical stability window.

Conclusion

In conclusion, Zn doped $Li_5La_3Nb_2O_{12}$ and $Li_6La_3ZrNbO_{12}$ were successfully synthesised through a conventional solid-state method. The relative density increased on Zn doping for both systems, up to 90% for the LLZNZ sample,

indicating that Zn is a good densification dopant for garnet materials. The conductivities in both systems were enhanced on Zn doping, with that of LLZNZ increasing to 2.1 x 10^{-4} Scm^{-1} at 25 ^{o}C which is ~ two orders more than that of $Li_6La_3ZrNbO_{12}$ under the same conditions. Therefore, this method represents a new way to both control the Li content and improve the relative density, and hence ionic conductivity of garnet solid state electrolyte materials for possible solid-state battery applications.

Acknowledgements

We would like to thank EPSRC (grant EP/R024006/1: ICSF Wave 1: GENESIS: Garnet Electrolytes for New Energy Storage Integrated Solutions) for financial support.

Conflict of Interest

The authors declare no conflict of interest.

References

1. Goodenough, J. B.; Park, K. S., The Li-Ion Rechargeable Battery: A Perspective. *J. Am. Chem. Soc.* **2013,** 135, (4), 1167-1176.

2. Tarascon, J.-M.; Armand, M., Issues and Challenges Facing Rechargeable Lithium Batteries. *Nature* **2001,** 414, (6861), 359-367.

3. Bruce, P. G.; Scrosati, B.; Tarascon, J. M., Nanomaterials for Rechargeable Lithium Batteries. *Angew. Chem. Int. Ed. Engl.* **2008,** 47, (16), 2930-46.

4. Manthiram, A.; Yu, X.; Wang, S., Lithium Battery Chemistries Enabled by

Solid-State Electrolytes. *Nat. Rev. Mater.* **2017,** 2, (4).

5. Zhang, Z.; Shao, Y.; Lotsch, B.; Hu, Y.-S.; Li, H.; Janek, J.; Nazar, L. F.; Nan, C.-W.; Maier, J.; Armand, M.; Chen, L., New Horizons for Inorganic Solid State Ion Conductors. *Energy Environ. Sci.* **2018,** 11, (8), 1945-1976.

6. Bruce, P. G.; West, A. R., The A-C Conductivity of Polycrystalline LISICON,

$Li_{2+2x}Zn_{1-x}GeO_4$, and a Model for Intergranular Constriction Resistances *J. Electrochem. Soc.* **1983,** 130.

7. Dong, B.; Jarkaneh, R.; Hull, S.; Reeves-McLaren, N.; Biendicho, J. J.; West, A. R., Synthesis, Structure and Electrical Properties of N-Doped Li_3VO_4. *J. Mater. Chem. A* **2016,** 4, (4), 1408-1413.

8. Dong, B.; Yan, J.; Walkley, B.; Inglis, K. K.; Blanc, F.; Hull, S.; West, A. R., Synthesis and Characterisation of the New Oxyfluoride Li^+ Ion Conductor, Li_5SiO_4F. *Solid State Ionics* **2018,** 327, 64-70.

9. M.A. Subramanian; R. Subramanian; A. Clearfield, Lithium Ion Conductors in the System $AB(IV)_2(PO_4)_3$ (B = Ti, Zr and Hf). *Solid State Ionics* **1986,** 18, 562.

10. V. Thangadurai; A.K. Shukla, J. G., New Lithium-Ion Conductors Based on the NASICON Structure. *J. Mater. Chem.* **1999,** 9, 739.

11. Y. Harada; T. Ishigaki; H. Kawai; Kuwano, J., Lithium Ion Conductivity of Polycrystalline Perovskite $La_{0.67-x}Li_{3x}TiO_3$ with Ordered and Disordered Arrangements of the A-Site Ions. *Solid State Ionics* **1998,** 108, 407.

12. Thangadurai, V.; Narayanan, S.; Pinzaru, D., Garnet-type Solid-State Fast Li Ion Conductors for Li Batteries: Critical Review. *Chem. Soc. Rev.* **2014,** 43, (13), 4714-4727.

13. Kanno, R.; Murayama, M., Lithium Ionic Conductor Thio-LISICON the Li_2S-GeS_2-P_2S_5 System. *J. Electrochem. Soc.* **2001,** 148.

14. Percival, J.; Apperley, D.; Slater, P. R., Synthesis and Structural Characterisation of the Li Ion Conducting Garnet-Related Systems, $Li_6ALa_2Nb_2O_{12}$ (A=Ca, Sr). *Solid State Ionics* **2008,** 179, (27-32), 1693-1696.

15. Zhao, Y.; Daemen, L. L., Superionic Conductivity in Lithium-Rich Anti-Perovskites. *J. Am. Chem. Soc.* **2012,** 134, (36), 15042-7.

16. Ramakumar, S.; Deviannapoorani, C.; Dhivya, L.; Shankar, L. S.; Murugan, R., Lithium Garnets: Synthesis, Structure, Li^+ Conductivity, Li^+ Dynamics and Applications. *Prog. Mater. Sci.* **2017,** 88, 325-411.

17. Thangadurai, V.; Kaack, H.; Weppner, W., Novel Fast Lithium Ion Conduction in Garnet-Type $Li_5La_3M_2O_{12}$ (M = Nb, Ta). *J. Am. Ceram. Soc.* **2003,** 86, (3), 437-440.

18. Cussen, E. J., Structure and Ionic Conductivity in Lithium Garnets. *J. Mater. Chem.* **2010,** 20, (25), 5167-5173.

19. Thangadurai, V.; Weppner, W., $Li_6ALa_2Ta_2O_{12}$ (A = Sr, Ba): Novel Garnet-Like Oxides for Fast Lithium Ion Conduction. *Adv. Funct. Mater.* **2005,** 15, (1), 107-112.

20. Percival, J.; Slater, P. R., Identification of the Li Sites in the Li Ion

Conductor, $Li_6SrLa_2Nb_2O_{12}$, through Neutron Powder Diffraction Studies. *Solid State Commun.* **2007,** 142, (6), 355-357.

21. Percival, J.; Kendrick, E.; Slater, P. R., . Synthesis and Conductivities of the Garnet-Related Li Ion Conductors, $Li_5Ln_3Sb_2O_{12}$ (Ln=La, Pr, Nd, Sm, Eu). *Solid State Ionics* **2008,** 179, (27-32), 1666-1669.

22. Howard, M. A.; Clemens, O.; Kendrick, E.; Knight, K. S.; Apperley, D. C.; Anderson, P. A.; Slater, P. R., Effect of Ga Incorporation on the Structure and Li Ion Conductivity of $La_3Zr_2Li_7O_{12}$. *Dalton Trans.* **2012,** 41, (39), 12048-12053.

23. Li, Y.; Han, J.-T.; Wang, C.-A.; Xie, H.; Goodenough, J. B., Optimizing Li^+ Conductivity in A Garnet Framework. *J. Mater. Chem.* **2012,** 22, (30).

24. Wolfenstine, J.; Ratchford, J.; Rangasamy, E.; Sakamoto, J.; Allen, J. L., Synthesis and High Li-Ion Conductivity of Ga-Stabilized Cubic $Li_7La_3Zr_2O_{12}$. *Mater. Chem. Phys.* **2012,** 134, (2-3), 571-575.

25. Howard, M. A.; Clemens, O.; Knight, K. S.; Anderson, P. A.; Hafiz, S.; Panchmatia, P. M.; Slater, P. R., Synthesis, Conductivity and Structural Aspects of $Nd_3Zr_2Li_{7-3x}Al_xO_{12}$. *J. Mater. Chem. A.* **2013,** 1, (44), 14013-14022.

26. Thompson, T.; Wolfenstine, J.; Allen, J. L.; Johannes, M.; Huq, A.; David, I. N.; Sakamoto, J., Tetragonal vs. Cubic Phase Stability in Al-free Ta Doped $Li_7La_3Zr_2O_{12}$ (LLZO). *J. Mater. Chem. A.* **2014,** 2, (33), 13431-13436.

27. Awaka, J.; Kijima, N.; Hayakawa, H.; Akimoto, J., Synthesis and Structure Analysis of Tetragonal $Li_7La_3Zr_2O_{12}$ with the Garnet-Related Type Structure. *J. Solid State Chem.* **2009,** 182, (8), 2046-2052.

28. Percival, J.; Kendrick, E.; Smith, R. I.; Slater, P. R., Cation Ordering in Li Containing Garnets: Synthesis and Structural Characterisation of the Tetragonal System, $Li_7La_3Sn_2O_{12}$. *Dalton Trans.* **2009**, (26), 5177-5181.

29. Awaka, J.; Kijima, N.; Kataoka, K.; Hayakawa, H.; Ohshima, K.-i.; Akimoto, J., Neutron Powder Diffraction Study of Tetragonal $Li_7La_3Hf_2O_{12}$ with the Garnet-Related Type Structure. *J. Solid State Chem.* **2010,** 183, (1), 180-185.

30. Larraz, G.; Orera, A.; Sanjuán, M. L., Cubic Phases of Garnet-Type $Li_7La_3Zr_2O_{12}$: The Role of Hydration. *J. Mater. Chem. A* **2013,** 1, (37), 11419-11428.

31. Truong, L.; Howard, M.; Clemens, O.; Knight, K. S.; Slater, P. R.; Thangadurai, V., Facile Proton Conduction in H^+/Li^+ Ion-Exchanged Garnet-Type Fast Li-Ion Conducting $Li_5La_3Nb_2O_{12}$. *J. Mater. Chem. A* **2013,** 1, (43), 13469-13475.

32. Brugge, R. H.; Hekselman, A. K. O.; Cavallaro, A.; Pesci, F. M.; Chater, R. J.; Kilner, J. A.; Aguadero, A., Garnet Electrolytes for Solid State Batteries: Visualization of Moisture-Induced Chemical Degradation and Revealing Its Impact on the Li-Ion Dynamics. *Chem. Mater.* **2018,** 30, (11), 3704-3713.

33. Pesci, Federico M.; Brugge, R. H.; Hekselman, A. K. O.; Cavallaro, A.; Chater, R. J.; Aguadero, A., Elucidating the Role of Dopants in the Critical Current Density for Dendrite Formation in Garnet Electrolytes. *J. Mater. Chem. A.* **2018,** 6, (40), 19817-19827.

34. Squires, A. G.; Scanlon, D. O.; Morgan, B. J., Native Defects and Their Doping Response in the Lithium Solid Electrolyte $Li_7La_3Zr_2O_{12}$. *Chem. Mater.* **2019,** 32, (5), 1876-1886.

35. Xiao, Y.; Wang, Y.; Bo, S.-H.; Kim, J. C.; Miara, L. J.; Ceder, G., Understanding Interface Stability in Solid-State Batteries. *Nat. Rev. Mater.* **2019,** 5, (2), 105-126.

36. Han, X.; Gong, Y.; Fu, K. K.; He, X.; Hitz, G. T.; Dai, J.; Pearse, A.; Liu, B.; Wang, H.; Rubloff, G.; Mo, Y.; Thangadurai, V.; Wachsman, E. D.; Hu, L., Negating Interfacial Impedance in Garnet-Based Solid-State Li Metal Batteries. *Nat. Mater.* **2017,** 16, (5), 572-579.

37. Dai, J.; Yang, C.; Wang, C.; Pastel, G.; Hu, L., Interface Engineering for Garnet-Based Solid-State Lithium-Metal Batteries: Materials, Structures, and Characterization. *Adv. Mater.* **2018,** 30, (48), e1802068.

38. Li, Y.; Chen, X.; Dolocan, A.; Cui, Z.; Xin, S.; Xue, L.; Xu, H.; Park, K.; Goodenough, J. B., Garnet Electrolyte with an Ultralow Interfacial Resistance for Li-Metal Batteries. *J. Am. Chem. Soc.* **2018,** 140, (20), 6448-6455.

39. Zhou, W.; Wang, Z.; Pu, Y.; Li, Y.; Xin, S.; Li, X.; Chen, J.; Goodenough, J. B., Double-Layer Polymer Electrolyte for High-Voltage All-Solid-State Rechargeable Batteries. *Adv. Mater.* **2019,** 31, (4), e1805574.

40. Yi, E.; Wang, W.; Kieffer, J.; Laine, R. M., Key Parameters Governing the Densification of Cubic-$Li_7La_3Zr_2O_{12}$ Li^+ Conductors. *J. Power Sources* **2017,** 352, 156-164.

41. Dong, B.; Driscoll, L. L.; Stockham, M. P.; Kendrick, E.; Slater, P. R., Low Temperature Synthesis of Garnet Solid State Electrolytes: Implications on Aluminium Incorporation in $Li_7La_3Zr_2O_{12}$. *Solid State Ionics* **2020,** 350.

42. Allen, J. L.; Wolfenstine, J.; Rangasamy, E.; Sakamoto, J., Effect of Substitution (Ta, Al, Ga) on the Conductivity of $Li_7La_3Zr_2O_{12}$. *J. Power Sources* **2012,** 206, 315-319.

43. Baek, S.-W.; Lee, J.-M.; Kim, T. Y.; Song, M.-S.; Park, Y., Garnet Related Lithium Ion Conductor Processed by Spark Plasma Sintering for All Solid State Batteries. *J. Power Sources* **2014,** 249, 197-206.

44. Ohta, S.; Komagata, S.; Seki, J.; Saeki, T.; Morishita, S.; Asaoka, T., All-Solid-State Lithium Ion Battery Using Garnet-Type Oxide and Li_3BO_3 Solid Electrolytes Fabricated by Screen-Printing. *J. Power Sources* **2013,** 238, 53-56.

45. Janani, N.; Deviannapoorani, C.; Dhivya, L.; Murugan, R., Influence of Sintering Additives on Densification and Li^+ Conductivity of Al Doped $Li_7La_3Zr_2O_{12}$ Lithium Garnet. *RSC Adv.* **2014,** 4, (93), 51228-51238.

46. Chen, Y.; Rangasamy, E.; Liang, C.; An, K., Origin of High Li^+ Conduction in Doped $Li_7La_3Zr_2O_{12}$. Garnets. *Chem. Mater.* **2015,** 27, (16), 5491-5494.

47. Hanc, E.; Zając, W.; Lu, L.; Yan, B.; Kotobuki, M.; Ziąbka, M.; Molenda, J., On Fabrication Procedures of Li-Ion Conducting Garnets. *J. Solid State Chem.* **2017,** 248, 51-60.

48. Azad, A.; Irvine, J., High Density and Low Temperature Sintered Proton

Conductor $BaCe_{0.5}Zr_{0.35}Sc_{0.1}Zn_{0.05}O_{3-\delta}$. *Solid State Ionics.* **2008,** 179, (19-20), 678-682.

49. Babilo, P.; Haile, S. M., Enhanced Sintering of Yttrium-Doped Barium Zirconate by Addition of ZnO. *J. Am. Ceram. Soc.* **2005,** 88, (9), 2362-2368.

50. Irvine, J. T. S.; Sinclair, D. C.; West, A. R., Electroceramics: Characterization by Impedance Spectroscopy. *Adv. Mater.* **1990,** 2, (3), 132-138.

51. Dong, B.; Hull, S.; West, A. R., Phase Formation, Crystallography, and Ionic Conductivity of Lithium Manganese Orthosilicates. *Inorg. Chem.* **2019,** 58, (1), 715-723.

Captions of figures and tables

Figure 1. XRD patterns of $Li_{5+3x}La_3Nb_{2-x}Zn_xO_{12}$: x = 0, 0.1 0.2, 0.3, 0.4 Triangle, diamond, circular and rectangle labels represent for $ZnNb_2O_6$, $LiNbO_3$, La_2O_3 and unknown peaks respectively.

Figure 2. Variation of lattice parameter a and volume V for $Li_{5+3x}La_3Nb_{2-x}Zn_xO_{12}$ with composition x.

Figure 3. (a) XRD patterns for $Li_6La_3ZrNbO_{12}$ and $Li_{6.6}La_3ZrNb_{0.8}Zn_{0.2}O_{12}$. (b) Observed, calculated and difference profiles from Rietveld refinement for $Li_6La_3ZrNbO_{12}$. (c) Observed, calculated and difference profiles from Rietveld refinement for $Li_{6.6}La_3ZrNb_{0.8}Zn_{0.2}O_{12}$.

Figure 4. EDX elemental mappings of $Li_{6.6}La_3ZrNb_{0.8}Zn_{0.2}O_{12}$.

Figure 5. Impedance data of $Li_{6.6}La_3ZrNb_{0.8}Zn_{0.2}O_{12}$. (a) Complex Z* plot (b) Spectroscopic plot of C’ (c) Spectroscopic plot of Y’

Figure 6. Arrhenius conductivity plots for Zn-doped $Li_5La_3Nb_2O_{12}$. Unit of activation energy is set as eV.

Figure 7. Arrhenius conductivity plots for Zn-doped $Li_6La_3ZrNbO_{12}$. Unit of

activation energy is set as eV.

Figure 8. CV of $Li_{6.6}La_3ZrNb_{0.8}Zn_{0.2}O_{12}$ with stainless-steel and Li metal as working and counter electrodes, at a scanning rate of 1 mVs^{-1}.

Table 1 Refined structural parameters for $Li_6La_3ZrNbO_{12}$ using XRD data.

Table 2 Refined structural parameters for $Li_{6.6}La_3ZrNb_{0.8}Zn_{0.2}O_{12}$ using XRD data.

Table 3. Relative densities for Zn-doped $Li_5La_3Nb_2O_{12}$ or $Li_6La_3ZrNbO_{12}$ pellets.

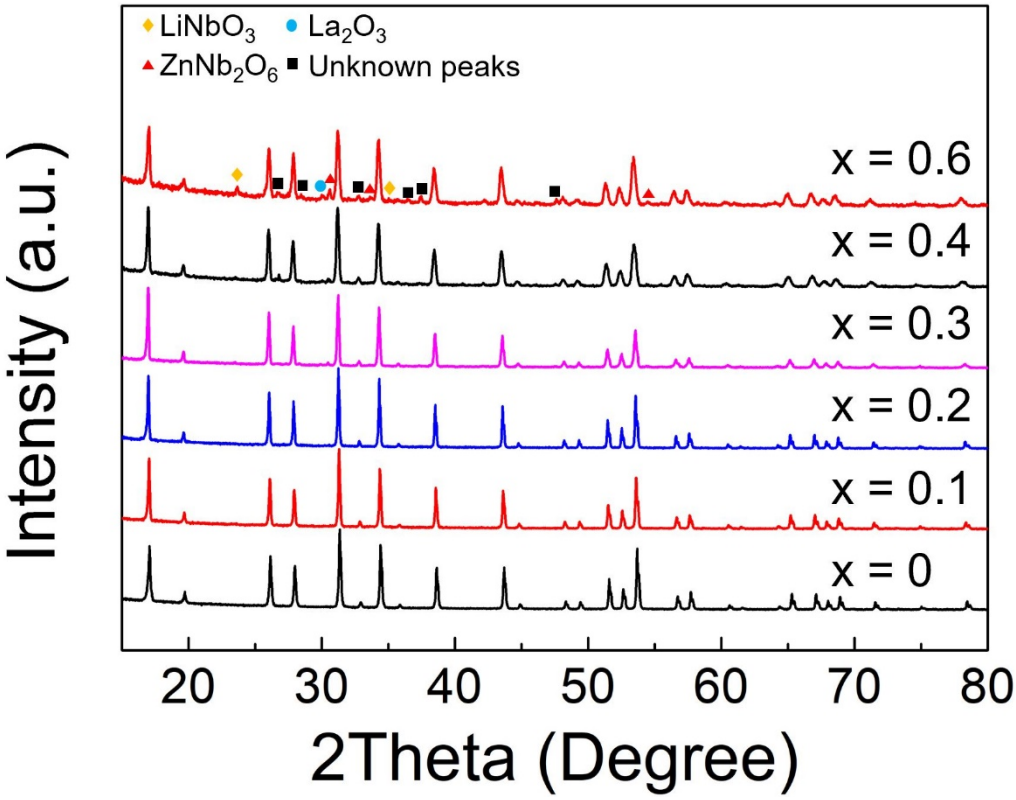
LiNbO3
La2O3
ZnNb2O6
Unknown peaks
x = 0.6
x = 0.4
x = 0.3
x = 0.2
x = 0.1
x = 0
Intensity (a.u.)
20
30
40
50
60
70
80
2Theta (Degree)

Figure 1

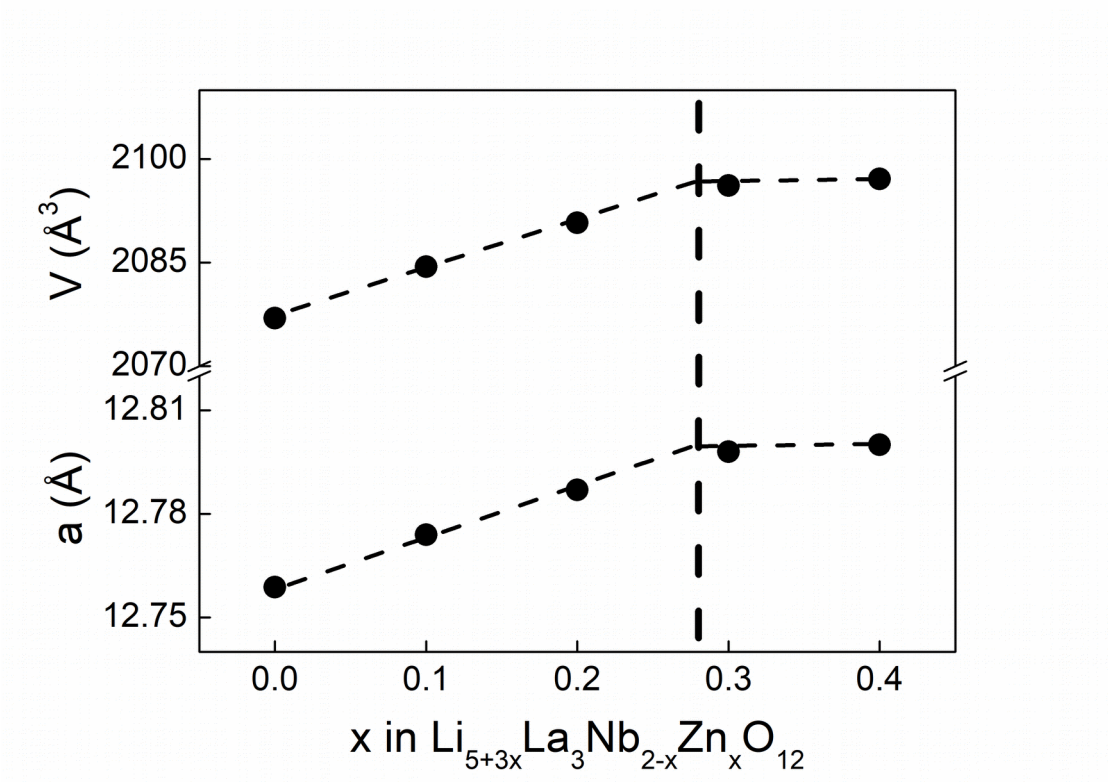
2100
2085
2070
V (Å3)
12.81
12.78
12.75
a (Å)
0.0
0.1
0.2
0.3
0.4
x in Li5+3xLa3Nb2-xZnxO12

Figure 2

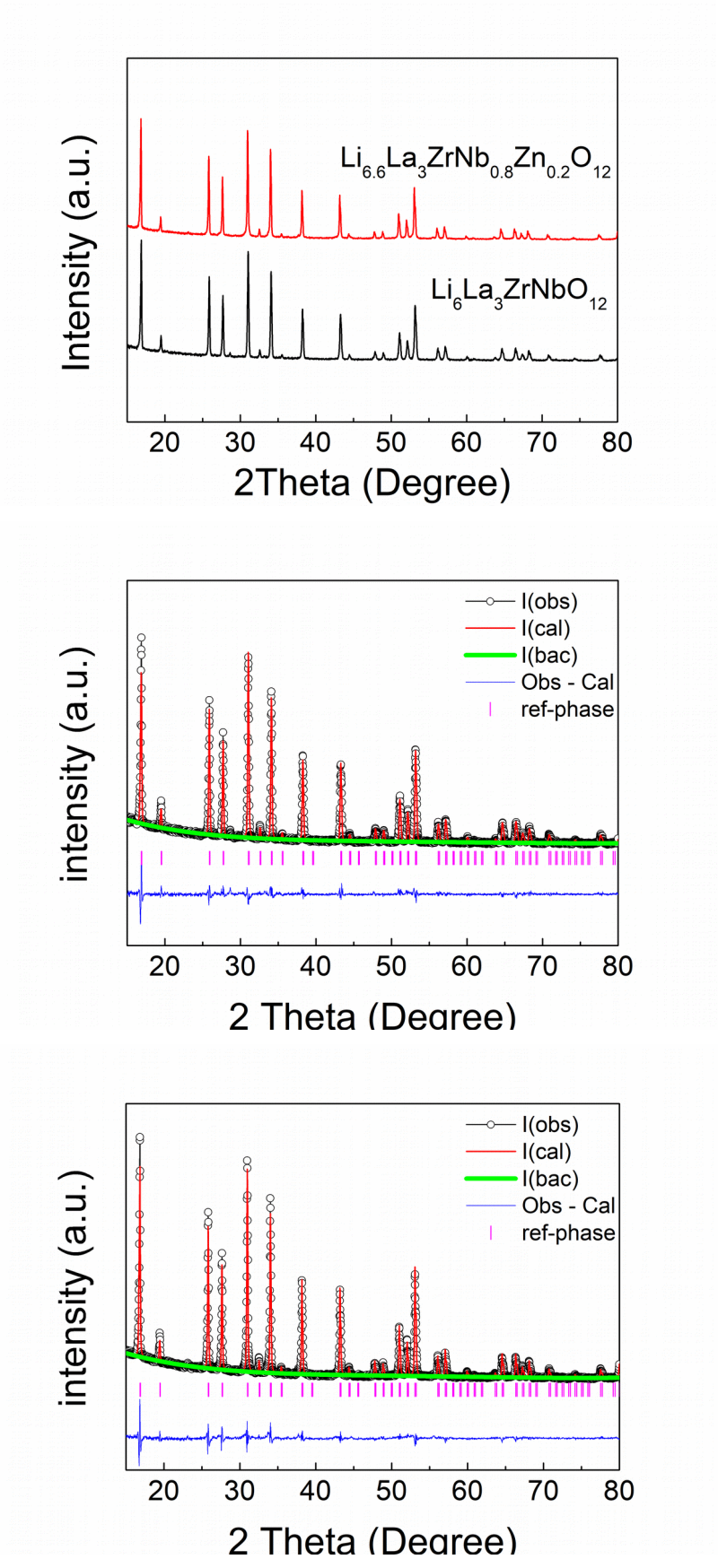
Intensity (a.u.)
Li6.6La3ZrNb0.8Zn0.2O12
Li6La3ZrNbO12
20
30
40
50
60
70
80
2Theta (Degree)
intensity (a.u.)
I(obs)
I(cal)
I(bac)
Obs - Cal
ref-phase
20
30
40
50
60
70
80
2 Theta (Degree)
intensity (a.u.)
I(obs)
I(cal)
I(bac)
Obs - Cal
ref-phase
20
30
40
50
60
70
80
2 Theta (Degree)

Figure 3

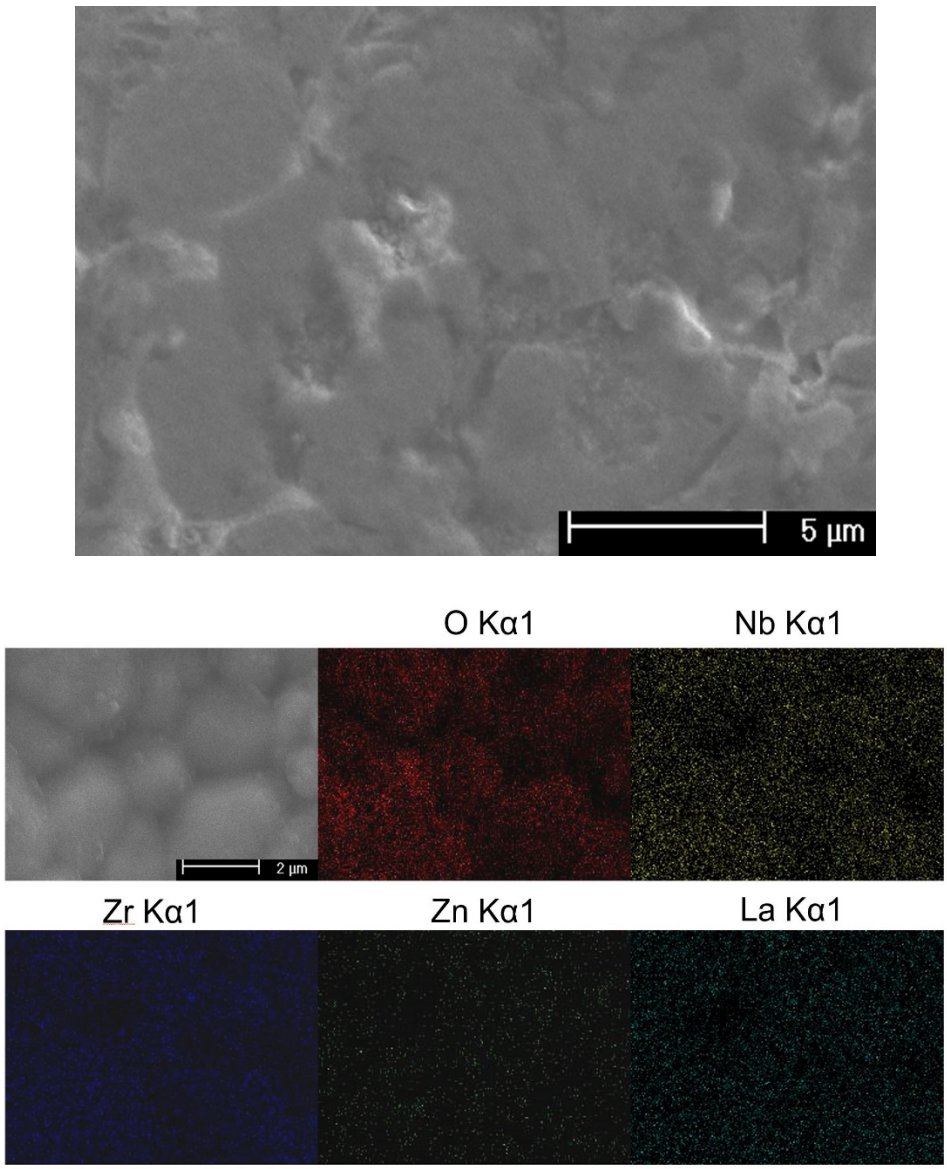

Figure 4

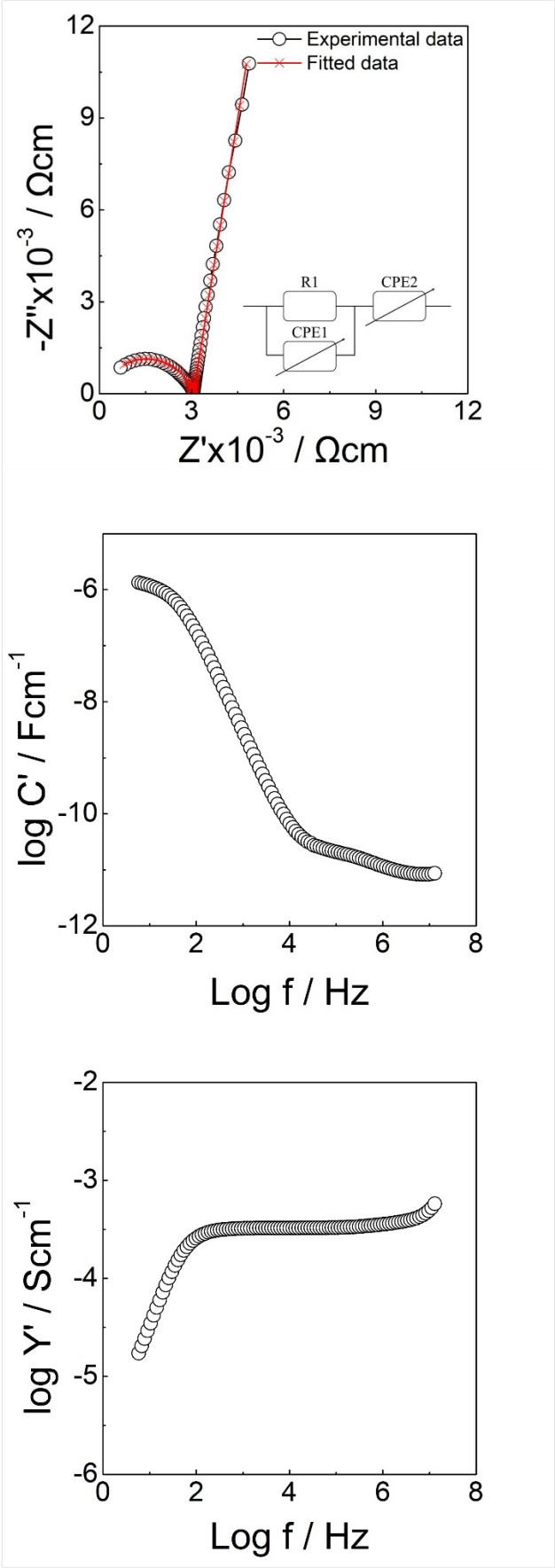
Experimental data
Fitted data
R1
CPE2
CPE1
-Z''x10-3 / Ωcm
Z'x10-3 / Ωcm
log C' / Fcm-1
Log f / Hz
log Y' / Scm-1
Log f / Hz

Figure 5

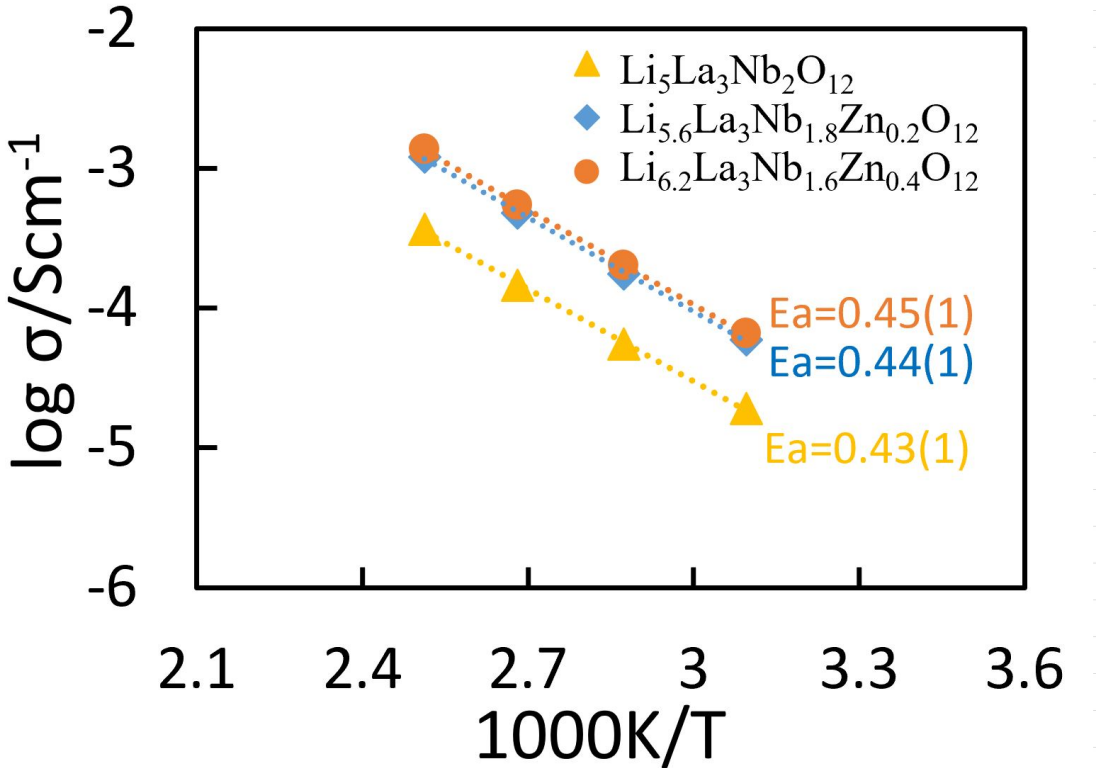
-2
-3
-4
-5
-6
log σ/Scm-1
2.1
2.4
2.7
3
3.3
3.6
1000K/T
Li5La3Nb2O12
Li5.6La3Nb1.8Zn0.2O12
Li6.2La3Nb1.6Zn0.4O12
Ea=0.45(1)
Ea=0.44(1)
Ea=0.43(1)

Figure 6

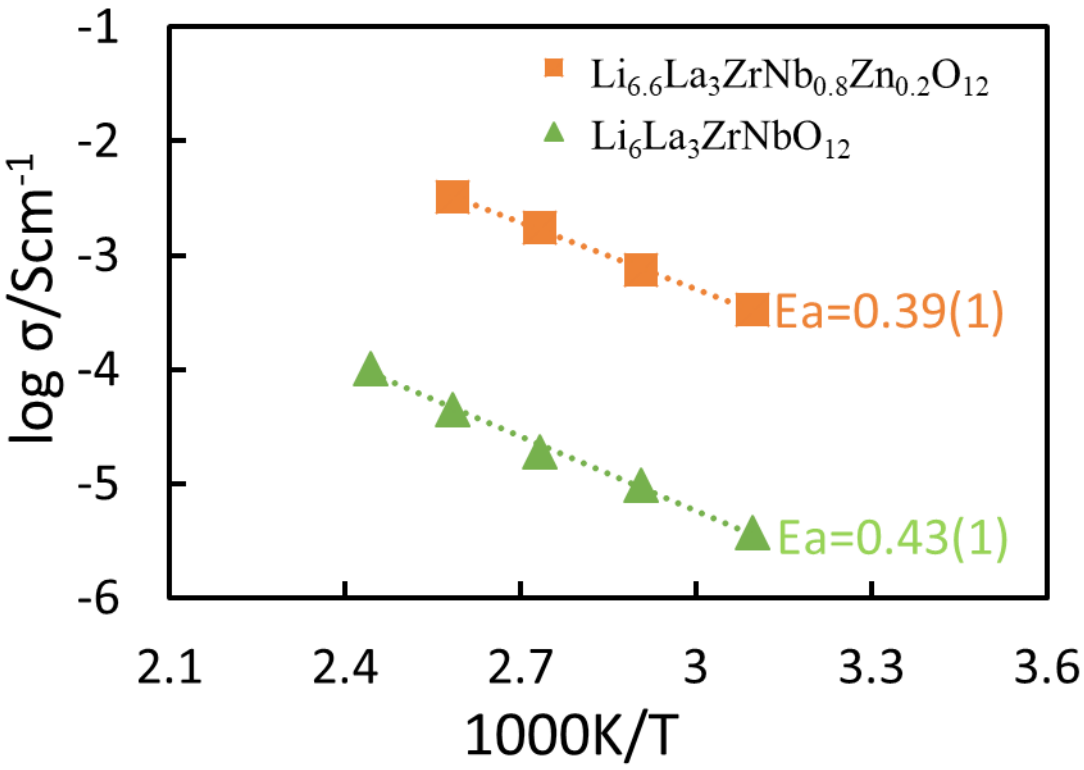
-1
-2
-3
-4
-5
-6
log σ/Scm-1
2.1
2.4
2.7
3
3.3
3.6
1000K/T
Li6.6La3ZrNb0.8Zn0.2O12
Li6La3ZrNbO12
Ea=0.39(1)
Ea=0.43(1)

Figure 7

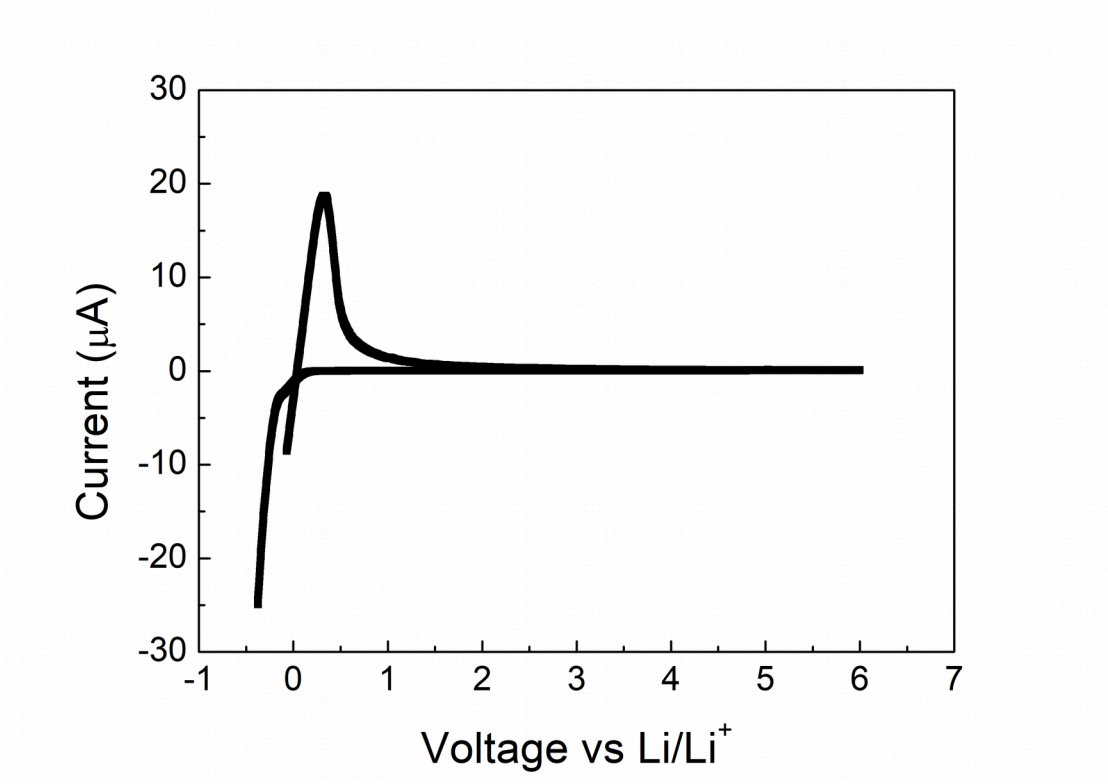

Figure 8

Table 1

Atom	*x*	*y*	*z*	Mult.	Occupancy	$u_{iso}\times100$ (Å^2)
La1	0.125	0	0.25	24	1	1.0(1)
Nb1	0	0	0	16	0.5	0.9(2)
Zr1	00	0	0	16	0.5	0.9
O1	0.2858(6)	0.1022(8)	0.1980(7)	96	1	2.3(4)
Li1	0.25	0.875	0	24	0.836	0.1
Li2	0.125	0.6798	0.5702	48	0.110	0.1
Li3	0.095	0.6818	0.5778	96	0.152	0.1

a = 12.8885(2)Å, V = 2140.98(8) Å^3

χ^2 = 2.538, R_{wp} = 9.28%, R_p = 7.45%

Table 2

Atom	*x*	*y*	*z*	Mult.	Occupancy	$u_{iso}\times100$ (Å^2)
La1	0.125	0	0.25	24	1	2.1(1)
Zr1	0	0	0	16	0.5	0.1
Nb1	0	0	0	16	0.40(1)	0.1
Zn1	0	0	0	16	0.10(1)	0.1
O1	0.2849(5)	0.1028(7)	0.1966(6)	96	1	4.4(4)
Li1	0.25	0.875	0	24	0.836	0.1
Li2	0.125	0.6798	0.5702	48	0.110	0.1
Li3	0.095	0.6818	0.5778	96	0.152	0.1

a = 12.9081(1)Å, V = 2150.71(5) Å^3

χ^2 = 3.755, R_{wp} = 9.81%, R_p = 8.06%

Table 3

Composition	Condition	Relative Density
$Li_5La_3Nb_2O_{12}$	1100/4h	61.0%
$Li_{5.6}La_3Nb_{1.8}Zn_{0.2}O_{12}$	1100/4h	87.1%
$Li_{6.2}La_3Nb_{1.6}Zn_{0.4}O_{12}$	1100/4h	87.2%
$Li_6La_3ZrNbO_{12}$	1100/6h	59.0%
$Li_{6.6}La_3Nb_{0.8}Zn_{0.2}ZrO_{12}$	1100/6h	90.3%